3988 *Chem. Mater.* **2010,** *22,* 3988–3994
DOI:10.1021/cm100705c

CHEMISTRY OF MATERIALS
Article

# Optimized Synthesis and Magnetic Properties of Intermetallic $Au_3Fe_{1-x}$, $Au_3Co_{1-x}$, and $Au_3Ni_{1-x}$ Nanoparticles

James F. Bondi,[†] Rajiv Misra,[‡,§] Xianglin Ke,[‡,§] Ian T. Sines,[†] Peter Schiffer,[‡,§] and Raymond E. Schaak*,[†,§]

[†]*Department of Chemistry,* [‡]*Department of Physics, and* [§]*Materials Research Institute, The Pennsylvania State University, University Park, Pennsylvania 16802*

*Received March 9, 2010. Revised Manuscript Received June 1, 2010*

Au and the 3d transition metals are immiscible under equilibrium conditions, but nonequilibrium alloys and intermetallic compounds of these elements are of interest for their potential multifunctional optical, catalytic, and magnetic properties. Here we report an optimized synthesis of intermetallic compounds with nominal compositions of $Au_3Fe_{1-x}$, $Au_3Co_{1-x}$, and $Au_3Ni_{1-x}$ as nanoparticles. Identification and optimization of the key synthetic variables (solvent, order of reagent addition, stabilizer, heating rate) led to the generation of nanoparticles with high phase purity and sample sizes of $>30$ mg, which is an order of magnitude larger than what was previously achievable. These intermetallic nanoparticles, which have diffraction patterns consistent with the $L1_2$ structure type, were characterized by powder XRD, TEM, EDS, electron diffraction, UV−visible spectroscopy, and SQUID magnetometry. Aliquot studies showed that $Au_3Fe_{1-x}$ formed through the initial nucleation of Au nanoparticles, followed by subsequent incorporation of Fe. Magnetic studies of powdered samples identified $Au_3Fe_{1-x}$ and $Au_3Co_{1-x}$ as superparamagnetic with $T_B = 7.9$ and 2.4 K, respectively. $Au_3Ni_{1-x}$ is paramagnetic down to 1.8 K.

## Introduction

Under equilibrium conditions, Au is immiscible with the magnetic 3d elements Fe, Co, and Ni.[1−3] However, the known catalytic and optical properties of Au, coupled with the ubiquitous magnetism exhibited by Fe, Co, Ni, and their compounds, suggests that alloys and intermetallics of these elements should produce interesting materials, including important multifunctional compounds.[4] Bulk-scale nonequilibrium alloys of Au and Fe prepared by arc melting with rapid quenching have been shown to exhibit interesting canonical spin-glass behavior.[5] Thin films of Au−Fe alloys exhibit ferromagnetic exchange coupling,[6] and chemically synthesized Au−Fe alloy nanoparticles exhibit tunable surface plasmon resonance frequencies and superparamagnetic blocking temperatures ($T_B$) across the $Au_{1-x}Fe_x$ solid solution.[7,8] Intermetallic $L1_0$-type AuFe has been artificially fabricated in thin film form by depositing and annealing alternating monolayers of Au and Fe, as well as vacuum annealing of Au nanoparticles overgrown with Fe via evaporation.[9−13] Bulk $Au_{1-x}Ni_x$ alloys prepared by induction melting and rapid quenching show composition-dependent magnetic behavior that ranges from paramagnetic to ferromagnetic.[14] Borohydride reduction of metal salts contained within dendrimer templates generated Au−Ni alloy nanoparticles,[15] and chemically synthesized Au−Ni alloy nanoparticles were used as precursors to Au-NiO/$SiO_2$ catalysts for CO oxidation.[16] Computational studies have identified $L1_2$-type intermetallic $Au_3Co$ as having interesting magnetic properties,[17,18] and Au−Co alloys have been successfully prepared using ion beam manipulation and coevaporation methods.[19,20] Recently, paramagnetic Au/Co

---

*Corresponding author. E-mail: schaak@chem.psu.edu.

(1) Liu, Y.; Ge, Y.; Yu, D. *J. Alloys Compd.* **2009**, *476*, 79–83.
(2) Okamoto, H.; Massalski, T. B.; Hasebe, M.; Nishizawa, T. *Bull. Alloy Phase Diagrams* **1985**, *6*(5), 449–454.
(3) Wang, J.; Lu, X.-G.; Sundman, B.; Su, X. *Calphad* **2005**, *29*, 263–268.
(4) Ferrando, R.; Jellinek, J.; Johnston, R. L. *Chem. Rev.* **2008**, *108*(3), 845–910.
(5) Taniguchi, T.; Yamanaka, K.; Sumioka, H.; Yamazaki, T.; Tabata, Y.; Kawarazaki, S. *Phys. Rev. Lett.* **2004**, *93*(24), 246605–4.
(6) Canet, F.; Bellouard, C.; Joly, L.; Mangin, S. *Phys. Rev. B* **2004**, *69*(9), 094402–11.
(7) Liu, H. L.; Wu, J. H.; Min, J. H.; Kim, Y. K. *J. Appl. Phys.* **2008**, *103*(7), 07D529–3.
(8) Chiang, I.-C.; Chen, D.-H. *Adv. Funct. Mater.* **2007**, *17*, 1311–1316.
(9) Takanashi, K.; Mitani, S.; Sano, M.; Fujimori, H.; Nakajima, H.; Osawa, A. *Appl. Phys. Lett.* **1995**, *67*(7), 1016–1018.
(10) Jaworowicz, J.; Maziewski, A.; Zablotskii, V.; Slezak, T.; Spiridis, N.; Korecki, J. *J. Magn. Magn. Mater.* **2004**, *272−276*, e555–e556.
(11) Ohtake, M.; Kirino, F.; Futamoto, M. *Jpn. J. Appl. Phys.* **2007**, *46*(37), L895–L897.
(12) Gavrilenko, V. I.; Wu, R. *J. Appl. Phys.* **1999**, *85*(8), 5112–5114.
(13) Sato, K.; Bian, B.; Hirotsu, Y. *Jpn. J. Appl. Phys.* **2002**, *41*, L1–L3.
(14) Kuentzler, R.; Kappler, J. P. *J. Phys. F: Met. Phys.* **1979**, *9*(2), 195–206.
(15) Auten, B. J.; Hahn, B. P.; Vijayaraghavan, G.; Stevenson, K. J.; Chandler, B. D. *J. Phys. Chem. C* **2008**, *112*(14), 5365–5372.
(16) Zhou, S.; Ma, Z.; Yin, H.; Wu, Z.; Eichhorn, B.; Overbury, S. H.; Dai, S. *J. Phys. Chem. C* **2009**, *113*(14), 5758–5765.
(17) Kong, Y.; Kong, L. T.; Liu, B. X. *J. Phys.: Condens. Matter* **2006**, *18*, 4345–4353.
(18) Sargolzaei, M.; Opahle, I.; Richter, M. *Phys. Status Solidi B* **2006**, *243*(1), 286–289.
(19) Yan, H. F.; Guo, H. B.; Shen, Y. X.; Li, J. H.; Liu, B. X. *Acta Mater.* **2006**, *54*, 5293–5304.
(20) Nabika, H.; Akamatsu, K.; Mizuhata, M.; Kajinami, A.; Deki, S. *J. Mater. Chem.* **2002**, *12*, 2408–2411.

bimetallic nanoparticles have been synthesized by reducing gold(III) chloride in the presence of premade Co nanoparticles.[21] Despite these reports, it remains a significant challenge to generate bulk-scale quantities of nonequilibrium intermetallics in the Au−Fe, Au−Co, and Au−Ni systems.

Recently, our group reported the first synthesis of $L1_2$-type intermetallics with nominal compositions of $Au_3Fe$, $Au_3Co$, and $Au_3Ni$,[22] which, based on elemental analysis, are best described as $Au_3Fe_{1-x}$, $Au_3Co_{1-x}$, and $Au_3Ni_{1-x}$. These nonequilibrium intermetallics were synthesized as colloidal nanoparticles using air-sensitive solution chemistry techniques. In this initial work, we described a synthetic protocol for accessing these nonequilibrium intermetallics, identified the $L1_2$ structure type, and proposed a reaction pathway that rationalized their formation using low-temperature solution chemistry methods. Property measurements were not reported because of known Au and $MO_x$ ($M$ = Fe, Co, or Ni) impurities that were present in the samples, as well as a limitation on the amount of isolatable sample (< 5 mg). Here, we describe an optimized synthesis procedure for the $Au_3M_{1-x}$ intermetallics that leads to larger quantities (> 30 mg) of highly crystalline nanoparticle products with minimal impurity levels. These investigations help to understand the key parameters that lead to optimized product formation and rationalize their role in accessing these nonequilibrium phases. We confirm and provide additional evidence for the reaction pathway, which involves the initial nucleation of Au nanoparticles followed by subsequent incorporation of Fe, Co, or Ni. Finally, we report studies of the magnetic properties, which show superparamagnetism in $Au_3Fe_{1-x}$ and $Au_3Co_{1-x}$ and paramagnetism down to 1.8 K in $Au_3Ni_{1-x}$.

## Experimental Section

**Materials.** $Fe(acac)_3$ (99.9+%), $Ni(acac)_2$ (95%), $Co(acac)_3$ (99.99+%), and oleyl amine (70% technical grade) were purchased from Sigma Aldrich. $HAuCl_4 \cdot 3H_2O$ (99.99%), *n*-butyllithium (*n*-BuLi, 2.5 M in hexane), and diphenyl ether (99% reagent grade) were purchased from Alfa Aesar. As-received $HAuCl_4 \cdot 3H_2O$, $Fe(acac)_3$, $Ni(acac)_2$, $Co(acac)_3$, and *n*-BuLi were transferred to and stored in an Ar-atmosphere glovebox. Diphenyl ether and oleyl amine were dried by heating to 110 °C for 1 h under vacuum to remove any excess water and transferred into the glovebox using a freeze−thaw degassing method, and stored with 3 Å molecular sieves. All experimental setups were prepared in an Ar-atmosphere glovebox and carried out under ultrahigh purity (UHP) Ar using standard Schlenk techniques. Work-ups were performed in air and ethanol was added to the reaction to quench any unreacted *n*-BuLi. The as-made particles are air-stable with no observable oxidation over at least one month.

**Synthesis.** A typical synthesis of the $Au_3Fe_{1-x}$ intermetallic nanoparticles is described below. Inside an Ar glovebox, 50 mg of $HAuCl_4 \cdot 3H_2O$ and 14.9 mg of $Fe(acac)_3$ were placed in a 50 mL 3-neck flask. Next, 10 mL of diphenyl ether and 250 $\mu$L of oleylamine were added to the 3-neck flask. The 3-neck apparatus was sealed using a condenser with an air-flow adapter on top, a thermometer adapter with mercury thermometer, and a 14/20 rubber septum. Also in the glovebox, 5 mL of diphenyl ether and 1.92 mL of 2.5 M *n*-BuLi (in hexane) were added to a 50 mL Schlenk flask and sealed with a rubber septum. Both the sealed 3-neck apparatus and sealed Schlenk flask were removed from the glovebox. The 3-neck apparatus was sonicated for ~30 min, or until all the metal salts were dissolved. At the same time, the Schlenk flask was connected to a Schlenk line under UHP Ar, and the hexanes were removed from the *n*-BuLi solution by vacuum for 30 min in order to prevent dangerous overpressure during injection. After that, the 3-neck apparatus was attached to the Schlenk line, flushed, and evacuated with Ar three times. The 3-neck apparatus was then filled with Ar and the reaction was performed under an Ar blanket. The 3-neck apparatus was heated to 80 °C over the course of 40 min and stirred for an additional 20 min, at which point the *n*-BuLi solution was released from vacuum, filled with Ar, and injected into the 3-neck apparatus using a metal syringe. Finally, the solution mixture in the 3-neck apparatus was heated to reflux at 248 °C over 75 min, after which the heating source was turned off and the reaction was allowed to cool to room temperature. The synthesis of $Au_3Ni_{1-x}$ and $Au_3Co_{1-x}$ are similar, substituting $Ni(acac)_2$ or $Co(acac)_3$ for $Fe(acac)_3$.

**Characterization.** Powder X-ray diffraction (XRD) data were collected on a Bruker Advance D8 X-ray diffractometer using Cu K$\alpha$ radiation. Lattice constants were refined using the Chekcell program. Transmission electron microscopy (TEM) images, high-resolution TEM, and selected area electron diffraction (SAED) patterns were collected using a JEOL-2010 $LaB_6$ microscope operating at 200 kV. Energy-dispersive X-ray spectroscopy (EDS) measurements were performed on a JEOL JSM 5400 scanning electron microscope and on a FEI Quanta 200 environmental scanning electron microscope operating in high vacuum mode. Samples for TEM imaging and SAED analysis were prepared by redispersing the $Au_3M_{1-x}$ intermetallic nanoparticles in toluene with one drop of oleic acid and drop coating onto a carbon coated copper grid. UV−visible spectroscopy data were collected using an Ocean Optics DH-2000-BAL spectrometer with quartz cuvettes. DC magnetization measurements were performed using a Quantum Design Superconducting Quantum Interference Device (SQUID) magnetometer. The samples were measured in powder form, loaded in a gelatin capsule. A magnetic field of 100 Oe was applied during the magnetization-temperature (MT) measurements. AC susceptibility measurements were performed using the ACMS option of the Quantum Design PPMS cryostat at temperatures down to 1.8 K and with a frequency range from 100 Hz to 10 kHz.

## Results and Discussion

**Optimizing the Synthesis of $Au_3Fe_{1-x}$.** In our initial report,[22] nanoparticles with nominal compositions of $Au_3M$ ($M$ = Fe, Co, Ni) were synthesized by reacting $HAuCl_4 \cdot 3H_2O$ and metal acac precursors with n-BuLi in hot octyl ether (solvent) in the presence of oleylamine (stabilizer). Subsequent investigations identified the solvent, order of reagent addition, stabilizer, heating rate, and Au:Fe ratio as the most important variables for optimization, and the influence of these parameters on product formation is detailed below.

---

(21) Cheng, G.; Hight Walker, A. R. *J. Magn. Magn. Mater.* **2007**, *311*, 31–35.

(22) Vasquez, Y.; Luo, Z.; Schaak, R. E. *J. Am. Chem. Soc.* **2008**, *130*(36), 11866–11867.

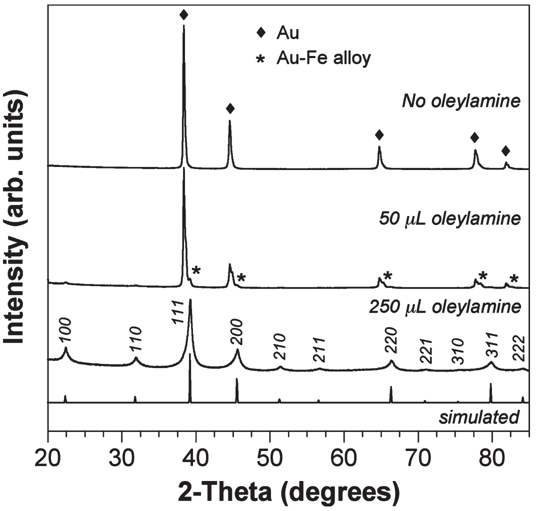

**Figure 1.** Powder XRD data showing the effect of varying the amount of oleylamine used in the synthesis of $Au_3Fe_{1-x}$ nanoparticles. A simulated XRD pattern for intermetallic $Au_3Fe_{1-x}$ is shown for comparison. Peaks marked with diamonds (♦) correspond to fcc Au, peaks marked with asterisks (*) correspond to an Au–Fe alloy, and indexed peaks correspond to intermetallic $Au_3Fe_{1-x}$.

The $Au_3M_{1-x}$ intermetallics nucleate in solution around 230 – 250 °C and begin decomposing to Au and $M$ above 260 °C. Thus, to better control the temperature and avoid impurity formation via overshooting 260 °C, the solvent was changed from octyl ether (BP = 286 °C) to diphenyl ether (BP = 259 °C). The diphenyl ether reaction mixture that contains all reagents refluxes at 248 °C, so thermal decomposition of $Au_3M_{1-x}$ into Au and $MO_x$ impurities ($MO_x$ formed from post-isolation oxidation of $M$) is minimized. This leads directly to samples with higher purity that are appropriate for both optical and magnetic characterization, because the plasmonic Au nanoparticle impurities and magnetic $MO_x$ impurities that would interfere with property measurements are minimized. Also, instead of injecting the metal salt solution into the n-BuLi solution as previously reported, we added the n-BuLi solution to the metal salt solution in order to better control the reaction stoichiometry.

Figure 1 highlights the effect of oleylamine concentration on product formation. Nominally, oleylamine serves as a surface stabilizing agent, and the fact that the XRD peaks broaden as more oleylamine is added is consistent with this role.[23] However, when oleylamine is completely eliminated from the reaction, only Au is produced, with no evidence of crystalline $Au_3Fe_{1-x}$, Fe, or $FeO_x$ phases. This indicates that oleylamine plays an integral role in the formation of $Au_3Fe_{1-x}$, rather than simply passivating the particles and truncating growth. When 50 μL of oleylamine is used, the product is predominantly Au, although a few small peaks ($2\theta_{111}$ = 39.0° and $2\theta_{200}$ = 45.3°) indicate the formation of a fcc Au–Fe alloy phase along with an even smaller amount of $Au_3Fe_{1-x}$ that is barely detectable by XRD. Increasing the amount of oleylamine to 250 μL results in the formation of $Au_3Fe_{1-x}$, which appears phase pure by XRD. These investigations imply that oleylamine is also serving as a mild reducing agent, and this role is important in the overall reaction.[23] In the absence of oleylamine, the $Au^{3+}$ has not been reduced to $Au^0$ prior to adding the n-BuLi at 80 °C, resulting in the rapid growth of large Au crystals when n-BuLi reduces $Au^{3+}$. In the presence of oleylamine, Au nanoparticles are formed prior to injection of n-BuLi at 80 °C, avoiding the direct reduction of $Au^{3+}$ by n-BuLi. Indeed, aliquot studies (described later in detail) show the presence of Au particles prior to n-BuLi injection, consistent with this hypothesis. The Au nanoparticles serve as seeds for the formation of $Au_3M_{1-x}$ upon reduction of the metal acac precursors with n-BuLi.

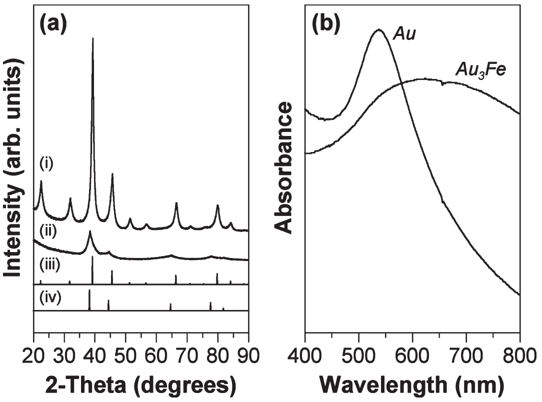

**Figure 2.** (a) Powder XRD data for (i) as-made $Au_3Fe_{1-x}$ nanoparticles and (ii) an aliquot taken at 80 °C prior to injection of n-BuLi. Simulated XRD patterns for intermetallic $Au_3Fe_{1-x}$ and fcc Au are shown in (iii) and (iv), respectively. (b) UV–visible absorption spectra for the aliquot taken at 80 °C (corresponding to Au nanoparticles) and the final product, intermetallic $Au_3Fe_{1-x}$, dispersed in toluene.

The rate of heating after injecting n-BuLi at 80 °C also influences phase formation and purity. Fast heating rates, e.g., heating from 80 to 248 °C over 40 min, result in the formation of crystalline Au or Au–Fe alloy impurities (see Figure S1 in the Supporting Information). Slower heating rates, e.g., heating from 80 to 248 °C over 75 min (2.24 °C/min), provide access to $Au_3Fe_{1-x}$ without detectable Au and Au–Fe alloy impurities (see Figure S1 in the Supporting Information). Even slower heating rates do not seem to affect the identity or purity of the final product, as long as the dwell temperature is 248 °C. We speculate that a slower heating rate facilitates the complete diffusion of Fe into the Au seeds.

**Formation and Characterization of $Au_3Fe_{1-x}$.** The reaction pathway involved in the formation of $Au_3Fe_{1-x}$ nanoparticles was studied by taking an aliquot immediately prior to the injection of n-BuLi at 80 °C and comparing it to the final product (248 °C) of the same reaction. Figures 2 and 3 show XRD, TEM, SAED, and UV–vis data for these two samples. The XRD pattern for the 80 °C aliquot (Figure 2a) shows predominantly Au [$a$ = 4.079(5) Å], along with noticeable small shoulders to the right of the Au peaks that suggest the formation of a small amount of an Au-rich Au–Fe alloy phase. TEM images (a) and (b) in Figure 3, corresponding to the particles isolated from the 80 °C aliquot, show the presence of Au

---

[23] Hiramatsu, H.; Osterloh, F. E. *Chem. Mater.* **2004**, *16*(13), 2509–2511.

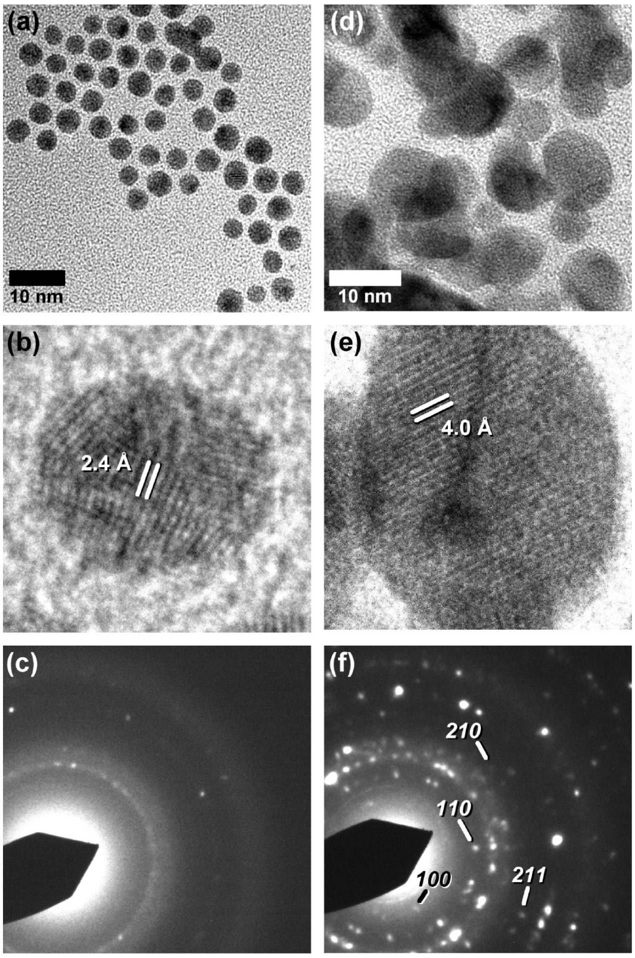

**Figure 3.** TEM images and SAED patterns corresponding to the 80 °C aliquot [(a−c) Au nanoparticles] and the final product [(d−f) intermetallic $Au_3Fe_{1-x}$ nanoparticles]. The HRTEM images highlight (b) the 111 plane of Au and (d) the 100 plane of $Au_3Fe_{1-x}$. The SAED pattern in (c) corresponds to fcc Au, whereas the SAED pattern in (f) clearly shows the superlattice peaks characteristic of the $L1_2$ structure.

seeds (6.0 ± 0.7 nm) formed from the reduction of $Au^{3+}$ with oleylamine, as described earlier. The HRTEM image in Figure 3b shows lattice fringes corresponding to $d$ = 2.4 Å, which is consistent with the 111 plane of Au. The UV−vis spectrum in Figure 2b shows that these Au-rich particles absorb around 540 nm, which is consistent with what is expected for Au nanoparticles in nonpolar solvents like hexane and toluene.[23] The SAED pattern (Figure 3c) confirms that the sample consists of fcc Au. Taken together, the data indicate that Au nanoparticle seeds containing a small amount of iron are formed in the early stages of the reaction prior to injection of n-BuLi.

After n-BuLi is injected and the sample is heated to 248 °C over 75 min, the final intermetallic product is formed. The XRD pattern for this product, taken from the same sample as the aliquot described above, is consistent with $L1_2$-type $Au_3Fe_{1-x}$ [$a$ = 3.984(2) Å] with no detectible impurities (Figure 2a). (At this point, we cannot rule out the possibility that interstitial impurities, including Li, help to stabilize the apparent $L1_2$ structure type.) The corresponding TEM image (Figure 3d) shows predominately spherical morphologies with some elongation and evidence of smaller particles likely attributed to a small amount of nonreacted Au seeds. The as-made nanoparticles have an average particle size of 11.3 ± 2.4 nm, based on the limiting diameter. A high-resolution TEM image of the $Au_3Fe_{1-x}$ particles (Figure 3e) shows lattice fringes with spacings of 4.0 Å, which matches the *d*-spacing expected for the 100 plane of $Au_3Fe_{1-x}$. UV−visible spectroscopy for the $Au_3Fe_{1-x}$ product (Figure 2b) shows an absorbance maximum around 620 nm, which represents a red shift of ~80 nm relative to the Au seeds. This red shift is consistent with reports for other Au−Fe alloy nanoparticles[7,8] and could be due to aggregation or a thin oxide shell on the $Au_3Fe_{1-x}$ particles. Observation of the superlattice peaks indicative of the $L1_2$ structure type by SAED (Figure 3f) confirms that the nanoparticles are intermetallic $Au_3Fe_{1-x}$. EDS measurements indicate an average composition of approximately 18% Fe and 82% Au (see Figure S2 in the Supporting Information), which corresponds to $x \approx 0.3$ in $Au_3Fe_{1-x}$ and is within experimental error of what was observed previously.[22] The slight Fe deficiency could possibly be attributed to vacancies or Li incorporation on the Fe sites.

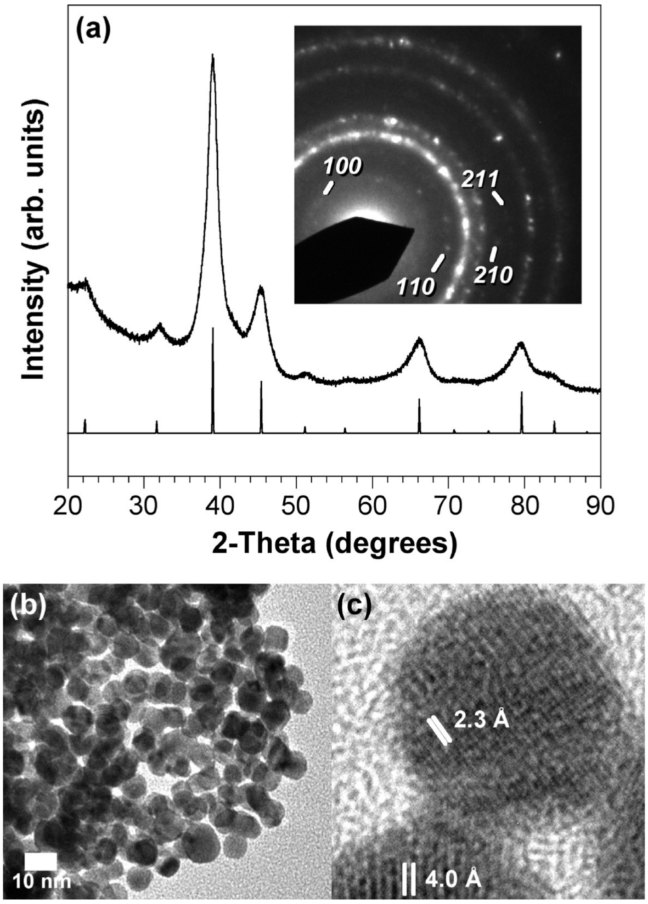

**Figure 4.** (a) Powder XRD data for intermetallic $Au_3Co$ nanoparticles, along with a simulated XRD pattern; (b) TEM image for the $Au_3Co_{1-x}$ nanoparticle; and (c) HRTEM image showing lattice fringes corresponding to both the 111 (2.3 Å) and 100 (4.0 Å) planes of intermetallic $Au_3Co_{1-x}$. The SAED pattern shown in the inset to panel (a) shows the superlattice reflections that correspond to the $L1_2$ structure type.

**Optimized Synthesis and Characterization of $Au_3Co_{1-x}$ and $Au_3Ni_{1-x}$.** Nanoparticles with nominal composition $Au_3Co_{1-x}$ were synthesized by substituting $Co(acac)_3$ for

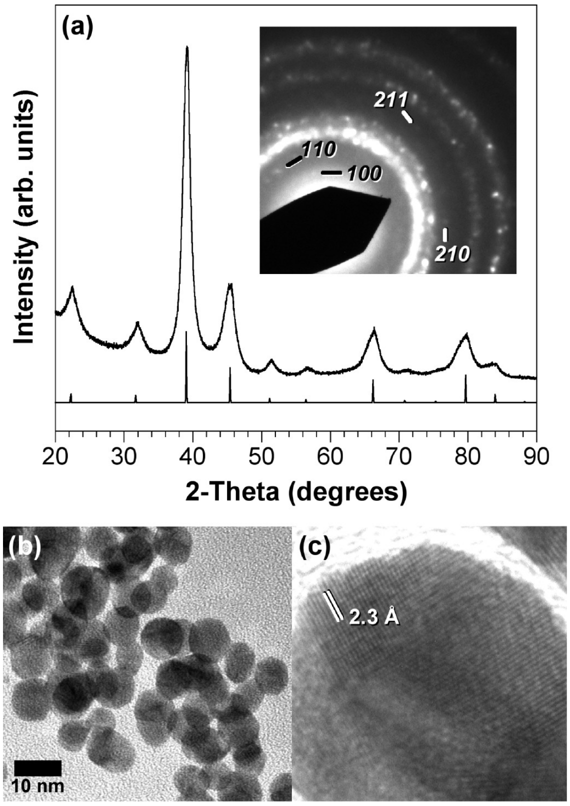

**Figure 5.** (a) Powder XRD data for intermetallic $Au_3Ni_{1-x}$ nanoparticles, along with a simulated XRD pattern; (b) TEM image for the $Au_3Ni_{1-x}$ nanoparticles; and (c) HRTEM image showing lattice fringes corresponding to the 111 plane of intermetallic $Au_3Ni_{1-x}$. The SAED pattern shown in the inset to panel (a) shows the superlattice reflections that correspond to the $L1_2$ structure type.

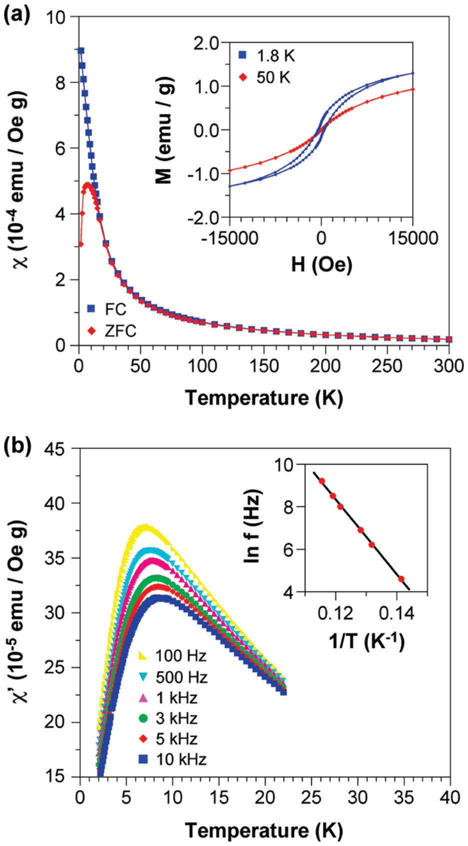

**Figure 6.** (a) FC and ZFC plots of DC susceptibility vs temperature (100 Oe) for $Au_3Fe_{1-x}$ nanoparticles. The inset shows a plot of DC magnetization vs field at 1.8 and 50 K. (b) Plot showing the real part of the AC susceptibility vs temperature for $Au_3Fe_{1-x}$ nanoparticles at different frequencies. The inset shows the Arrhenius plot of ln(*f*) vs inverse temperature.

Fe(acac)$_3$ using the optimized method described for $Au_3Fe_{1-x}$ above. Figure 4a shows the XRD pattern for $Au_3Co_{1-x}$ [$a$ = 4.003(3) Å]. The XRD and SAED patterns (Figure 4a) match those expected for the $L1_2$ structure type, including the characteristic superlattice peaks. A representative TEM image (Figure 4b) shows generally spherical particles with an average size of 11.9 ± 1.3 nm. A high-resolution TEM image of the $Au_3Co_{1-x}$ particles shows lattice fringes corresponding to both the 100 ($d$ = 4.0 Å) and 111 ($d$ = 2.3 Å) planes of $Au_3Co_{1-x}$. Taken together, the XRD, SAED, and HRTEM data confirm the $L1_2$ structure type. EDS data shows only 5−10% Co in the sample ($x \approx 0.7$ in $Au_3Co_{1-x}$), indicating significant amounts of vacancies or defect sites, or possibly incorporation of light elements such as carbon or lithium to help stabilize the $L1_2$ structure.

Nanoparticles with nominal composition $Au_3Ni_{1-x}$ were synthesized using the same optimized method described for $Au_3Fe_{1-x}$ and $Au_3Co_{1--x}$, using Ni(acac)$_2$ as the metal precursor. Figure 5a shows the XRD pattern for $Au_3Ni_{1-x}$ [$a$ = 3.996(6) Å], which shows no observable crystalline impurities. A representative TEM image (Figure 5b) shows particles of spherical morphology with an average size of 9.7 ± 1.7 nm. A high-resolution TEM image of the $Au_3Ni_{1-x}$ particles (Figure 5c) shows lattice fringes with spacings of 2.3 Å, which matches what is expected for the 111 plane of $Au_3Ni_{1-x}$. The SAED pattern (Figure 5a) also matches that expected for the $L1_2$ structure type, including observation of the characteristic superlattice peaks. EDS data indicates 10−15% Ni in the sample ($x \approx 0.5$ in $Au_3Ni_{1-x}$). Analogous to $Au_3Co_{1-x}$, this suggests the presence of vacancies or stabilization of the structure via interstitial carbon, lithium, etc. Interestingly, washing the intermetallic $Au_3Ni_{1-x}$ nanoparticles with ethanol does not change their crystal structure or composition. This is in contrast to previous reports of Au−Ni alloy nanoparticles synthesized using a similar method, which leach Ni in the presence of ethanol.[16] This suggests that the ordered intermetallic structure imparts additional stability on the Au−Ni nanoparticles, which bodes well for enhanced stability under catalytically relevant conditions.

**Magnetic Characterization of $Au_3Fe_{1-x}$, $Au_3Ni_{1-x}$, and $Au_3Co_{1-x}$.** The temperature dependence of the field-cooled (FC) and zero-field-cooled (ZFC) branches of the DC susceptibility in a field of 100 Oe is shown in Figure 6a for $Au_3Fe_{1-x}$ and Figure 7a for $Au_3Co_{1-x}$. In both cases, the ZFC branch exhibits a maximum while the FC branch increases monotonically with decreasing temperature. We take the maximum in the ZFC data as evidence of a blocking transition associated with an assembly of particles that exhibit superparamagnetic behavior.[24]

---

(24) Bandyopadhyay, M.; Dattagupta, S. *Phys. Rev. B* **2006**, *74*(21), 214410–7.

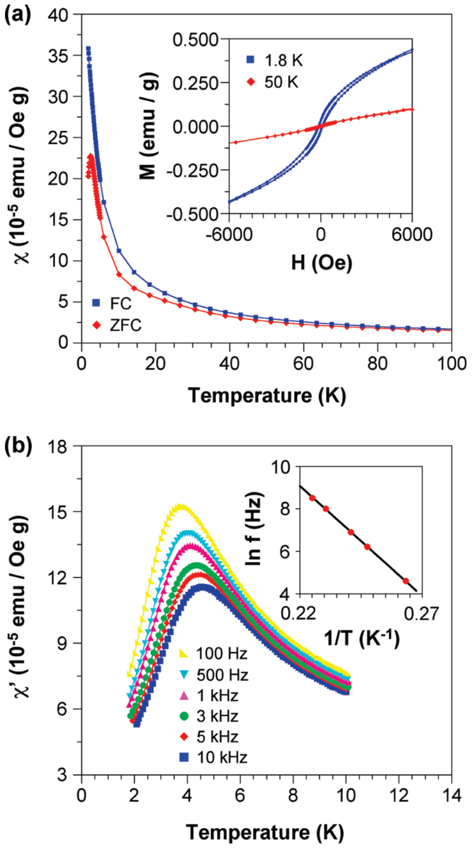

**Figure 7.** (a) FC and ZFC plots of DC susceptibility vs temperature (100 Oe) for $Au_3Co_{1-x}$ nanoparticles. The inset shows a plot of DC magnetization vs field at 1.8 and 50 K. (b) Plot showing the real part of the AC susceptibility vs temperature for $Au_3Co_{1-x}$ nanoparticles at different frequencies. The inset shows the Arrhenius plot of ln(*f*) vs inverse temperature.

The maximum in the data defines a blocking temperature, $T_B$, which we observe to be 7.9 and 2.4 K for $Au_3Fe_{1-x}$ and $Au_3Co_{1-x}$, respectively. The insets to Figure 6a and 7a show the magnetization as a function of magnetic field (*M* vs *H*) for $Au_3Fe_{1-x}$ and $Au_3Co_{1-x}$ above (50 K) and below (1.8 K) $T_B$, and the open hysteresis loops at 1.8 K are consistent with expectations for behavior below a blocking transition. The fact that the FC and ZFC curves do not fully converge above $T_B$ could possibly result from dipolar interactions among nanoparticles,[25] weak ferromagnetism arising from vacancies and defects, or the presence of small quantities of elemental Co that are below the detection limit of XRD and TEM.

Further confirmation of superparamagnetic behavior in $Au_3Fe_{1-x}$ and $Au_3Co_{1-x}$ is obtained from measurements of the temperature dependence of the AC susceptibility. Figures 6b and 7b show plots of $\chi'$ (the real part of the AC susceptibility) as a function of temperature in an AC field of 10 Oe at various frequencies for $Au_3Fe_{1-x}$ and $Au_3Co_{1-x}$, respectively. The peak position of the susceptibility curve, $T_f$, moves to higher temperatures with increasing frequency, as expected for a blocking transition. The temperature dependence of the peak position, displayed in the inset to Figures 6b and 7b, shows compliance with an Arrhenius law for thermal excitation for superparamagnetic materials, $\tau = \tau^* \exp(E/k_B T)$. For $Au_3Fe_{1-x}$, $1/\tau^* = 6.7 \times 10^{12}$ Hz and $E_a/k_B = 177(3)$ K. For $Au_3Co_{1-x}$, $1/\tau^* = 7 \times 10^{13}$ Hz and $E_a/k_B = 103.6(7)$ K. These fit parameters are consistent with previously studied superparamagnets.[26,27] The frequency shift of the peak $\Delta T_f/T_f$ [$\Delta \log \nu$] offers a good criterion for distinguishing a canonical spin glass from a superparamagnet. The magnitude of the frequency shift for a superparamagnet is large compared to that for a spin glass.[28−31] For $Au_3Fe_{1-x}$, the frequency shift $\Delta T_f/T_f$ [$\Delta \log \nu$] is 0.11, which is an order of magnitude larger than for the canonical spin-glass AuFe, for which the frequency shift is 0.010.[32] For $Au_3Co_{1-x}$, the frequency shift is 0.10, whereas canonical spin glasses typically have frequency shifts in the range 0.005−0.010. Taken together, the data strongly suggest superparamagnetism in the $Au_3Fe_{1-x}$ and $Au_3Co_{1-x}$ nanoparticles.

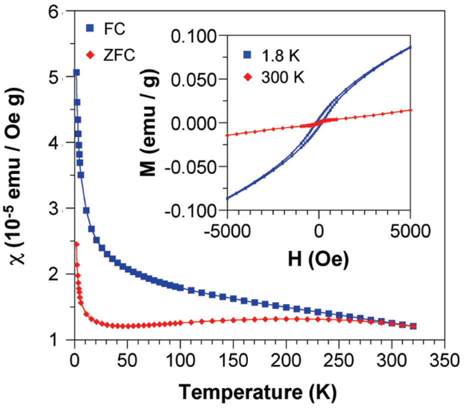

**Figure 8.** FC and ZFC plots of DC susceptibility vs temperature (100 Oe) for $Au_3Ni_{1-x}$ nanoparticles. The inset shows a plot of DC magnetization vs field at 1.8 and 300 K.

A plot of DC susceptibility vs temperature for the $Au_3Ni_{1-x}$ nanoparticles, measured in a field of 100 Oe, is shown in Figure 8. The data suggest the presence of two subsystems in the sample: one component with small particles that are either weakly paramagnetic or have a blocking temperature below 1.8 K and a second component that is weakly ferromagnetic up to room temperature, such as amorphous nickel metal. There is a separation of the FC and ZFC branches up to room temperature, and the ZFC curve shows a broad hump. As for the $Au_3Co_{1-x}$ sample, this could possibly be due to dipolar interactions among nanoparticles,[25] weak surface ferromagnetism, or small amounts of magnetic impurities below the detection limit. The inset to Figure 8 shows

---

(25) Frankamp, B. L.; Boal, A. K.; Tuominen, M. T.; Rotello, V. M. *J. Am. Chem. Soc.* **2005**, *127*, 9731–9735.

(26) Wang, S.; Zuo, J.-L.; Gao, S.; Song, Y.; Zhou, H.-C.; Zhang, Y.-Z.; You, X.-Z. *J. Am. Chem. Soc.* **2004**, *126*, 8900–8901.

(27) Xiao, G.; Liou, S. H.; Levy, A.; Taylor, J. N.; Chien, C. L. *Phys. Rev. B* **1986**, *34*, 7573–7577.

(28) Mulder, C. A. M.; van Duyneveldt, A. J.; Mydosh, J. A. *Phys. Rev. B* **1981**, *23*(3), 1384–1396.

(29) Binder, K.; Young, A. P. *Rev. Mod. Phys.* **1986**, *58*(4), 801–976.

(30) Mydosh, J. A. *Spin Glasses: An Experimental Introduction*; Taylor and Francis: London, 1993.

(31) Lu, J. J.; Lu, Y. M.; Lee, M. K.; Mo, T. S.; Jang, L. Y. *J. Magn. Magn. Mater.* **2006**, *305*(1), 259–263.

(32) Lundgren, L.; Svedlindh, P.; Beckman, O. *J. Phys. F.: Met. Phys.* **1982**, *12*, 2663–2673.

M vs H curves at 1.8 and 300 K. The M(H) data at 300 K (showing weak ferromagnetism) is presumably due to small quantities of an impurity phase that is below the detection limit of XRD or TEM. It is possible that blocking behavior may occur at temperatures below the limit of our measurement,[33] but we see no evidence of superparamagnetism in our samples. It is worth noting that the total moment observed in the M(H) data for all of the samples is below that which would be expected for full moments of the Fe, Co, and Ni associated with $x = 0$ compositions. We attribute this to some fraction of the transition metal atoms not contributing to the magnetism, presumably because of the nonzero values of $x$ and the complex associated local effects on the magnetism.

## Conclusions

In conclusion, we have described an optimized synthetic route to nonequilibrium intermetallic nanoparticles with nominal compositions of $Au_3Fe_{1-x}$, $Au_3Co_{1-x}$, and $Au_3Ni_{1-x}$. The $Au_3Fe_{1-x}$ and $Au_3Co_{1-x}$ nanoparticles are superparamagnetic with $T_B = 7.9$ and 2.4 K, respectively, whereas $Au_3Ni_{1-x}$ is weakly paramagnetic down to 1.8 K. The optimal synthesis exploits the key variables that maximize the formation of the desired intermetallic phases and minimize impurities: a solvent that refluxes below the $Au_3M_{1-x}$ decomposition temperature, an amine-based stabilizer that also acts as a weak reducing agent to generate Au nanoparticle seeds in situ, and a slow heating rate to ensure complete diffusion of the 3d element into the Au nanoparticle seeds. In addition to generating samples with high phase purity, this optimized synthesis yields greater than 30 mg of product, which is large enough for property studies and is an order of magnititude larger than previous methods for making these and related phases. We anticipate that these optimization efforts will also be applicable to other nonequilibrium solids formed using similar solution chemistry methods, particularly with respect to phase purity and scale-up.

**Acknowledgment.** This work was supported by the U.S. Department of Energy (DE-FG02-08ER46483), a DuPont Young Professor Grant, and a Camille Dreyfus Teacher-Scholar Award. R.M., X.K., and P.S. thank the Penn State MRSEC (DMR-0820404) and NSF (DMR-0701582) for funding. Electron microscopy was performed at the Electron Microscopy Facility at the Huck Institute for Life Sciences and at the Penn State Materials Research Institute. The authors acknowledge use of facilities at the PSU site of the NSF NNIN, and thank Trevor Clark and Josh Maier of the Materials Research Institute for assistance with the TEM imaging.

**Supporting Information Available:** Additional XRD and EDS data (PDF). This material is available free of charge via the Internet at http://pubs.acs.org.

---

(33) Chen, X.; Bedanta, S.; Petracic, O.; Kleemann, W.; Sahoo, S.; Cardoso, S.; Freitas, P. P. *Phys. Rev. B* **2005**, *72*(21), 214436–5.